ETH
Eidgenössische Technische Hochschule Zürich
Swiss Federal Institute of Technology Zurich

PAUL SCHERRER INSTITUT
PSI

Orbit Jitter Analysis

Semester Thesis

Department of Physics

ETH Zurich

written by

Veronika Senn

supervised by

Dr. A. Adelmann (ETH)

scientific supervisor

Dr. S. Reiche (PSI)

June 7, 2023

Abstract

SwissFEL produces electron bunches and accelerates them to near relativistic energies. Orbit jitters manifest in shot-to-shot variations of the beam position. Since fluctuations across the beamline are strongly correlated, principal component analysis (PCA) can be used to identify collective jitter sources. This semester project developed a python tool to collect beam position data and perform PCA as well as frequency component analysis on the data set. The dominance of the 50 Hz frequency amplitude across the beamline indicated that much of the variance throughout the beamline can be attributed to the main power supply to SwissFEL and its influence on the bunch production rate. The PCA output one main jitter source accounting for most of the total jitter. It was identified as energy jitter and its increased contribution in the second bunch compressor and energy colimator of SwissFEL imply a dispersion leakage in those sections or the linacs as jitter sources.

1 Introduction

Free-electron lasers (FEL) use a beam of electrons accelerated to relativistic energies as a gain medium in order to produce intense and coherent X-ray pulses. The wavelengths are small enough to perform X-ray diffraction and observe matter at the spatial and temporal scale of atomic processes. To induce those X-ray emissions, the accelerated electrons are made to interact with an alternating magnetic field generated by undulators. SwissFEL is a compact and cost-effective FEL facility located at the Paul Scherrer Institute (PSI) in Villigen. It contains two beam lines of different X-ray regimes, delivering hard X-rays at 0.1-0.7 nm as well as soft X-ray radiation of 0.65-5 nm.

In order to ensure optimal performance, the straightness of the electron orbit needs to be sustained throughout the beam lines. However, beam jitters cause shot to shot variations in the beam properties. Amongst other things, jitter induced relative energy deviations or transversal displacements from the reference orbit degrade the performance. However, jitter sources are typically small in numbers and the system responds to one of them with a characteristic imprinting in the measured orbits.

Instead of regarding orbit deviations at each longitudinal position individually, a correlation analysis across the beam line allows for the observation of collective movements of variations. For that purpose, beam position measurements can be used to perform principal component analysis (PCA). This method outputs eigenvectors to describe a system's collective response to jitter in order of the magnitude of their corresponding eigenvalues. In the framework of this semester project, a PCA application has been developed. The application can be used to display shot distributions, frequency amplitude developments and key aspects of the PCA by either employing existing data sets or by acquiring new data through current beam operations. The analysis tool allows for conclusions about possible jitters sources and their propagation throughout both beamlines at SwissFEL.

2 Background

A free-electron laser is a type of electron accelerator that outputs bright burst of X-rays at periodic intervals. The radiation is spatially coherent and ultrashort in duration, with a typical pulse duration below 35 fs. At the time of writing this report, SwissFEL consists of two beamlines. The hard X-ray beamline Aramis operates with wavelength as small as 1 Å and took up regular user operation in 2019 [1]. The soft X-ray beamline Athos on the other hand produces radiation in between 0.65 and 5.0 nm and was put into operation in 2021. SwissFEL works with a two-bunch operation mode and as can been seen in Figure 1, the two lines share a common acceleration and beam focus infrastructure up until the fast bunch separation system. There one bunch is redirected in the Athos-specific beamline structures at around 3 GeV [2]. Electron bunches for the Aramis line on the other hand are subjected to further acceleration until they reach an energy of 5.8 GeV.

SwissFEL generally consists of five functional parts. Electron production takes place in the injector. A photocathode RF gun produces electron bunches of about 200 pC at low energy spread and emittance via the photoelectric effect [1]. The two bunches for the two lines are output at 100 Hz and with a 28 ns spacing in between. The acceleration section consists of two subsequent compositions of bunch compressor and linear accelerator (linac). Because hard X-rays require higher energy electrons, a third linac accelerates the electron bunches for the Aramis line right after a septum magnet in the switch-yard extracts the Athos bunches from the main beamline. Photon production is carried out in the undulators, the periodic arrangement of permanent magnets with alternating polarisation. Due to the induced curved trajectory, the

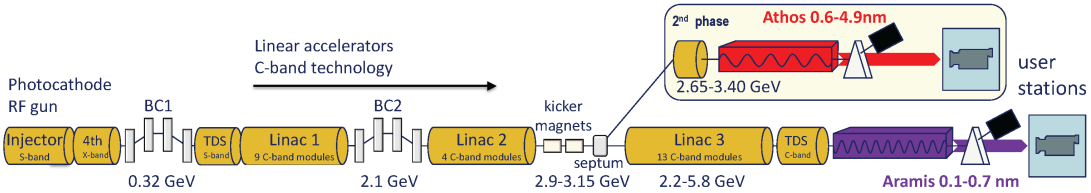

Figure 1: Composition schematic of SwissFEL. The figure is taken from [1].

accelerated electrons start to emit synchrotron radiation, which is mostly directed forward. Since the radiation advances faster than the wiggling electron, the photons interact with downstream electrons, causing them to accelerate or decelerate depending on their position with respect to the radiation phase. This process results in electron microbunching, which introduces a degree of coherence with emission levels above the spontaneous radiation. This self-amplified spontaneous emission (SASE) is the characteristic FEL mechanism to produce the desired X-radiation. The optics section of the beam line then prepares the output X-rays for the use in the last part, the experimentation stations.

2.1 Beam Position Monitors

In order to provide the best possible FEL performance, the electron beam trajectory needs to be stabilised. This reduces transverse wakefield effects and residual dispersion by properly aligning the orbit through the accelerating cavities and corrections of quadrupole magnet strengths controlling the dispersion in the acceleration section [2]. Furthermore, the undulators require a straightness of the electron orbit of a few microns over a length of up to 65 m to preserve the overlap of electron and photon beams. For this purpose, the beam orbit can be determined through the beam position monitors (BPM).

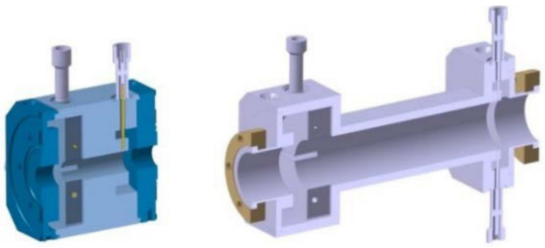

Figure 2: CBPM16 (left) and CBPM38 (right), two of the three BPM models installed at SwissFEL. Figure taken from [3].

The BPMs used at SwissFEL are based on dual resonator pickups [3]. Three different types are used throughout the beamline. The low loaded quality factor (Q_L) and 3.3 GHz cavity BPM models CBPM38 and CBPM16 are installed in most of the machine sections, whereas the high-Q_L, 4.9 GHz CBPM8 models can be found in the undulator sections. Note that the number in the type name refers to the inner diameter of the vacuum chamber (aperture size) in millimeters. Apart from beam position measurement in the dipole cavities, where a non-zero signal indicates an offset to the electro-magnetic axis of the cavities, signals from a monopole cavity can also monitor the bunch charges. The latter information can then in turn be used to normalise dipole cavity signals. If the beamline is taken to be aligned along the z-axis, the BPMs can determine

the position of the beam along the x- and y-axis. The position noise is smaller than 10 or 1 μm, depending on the model.

The data for the PCA produced by the BPMs is readout through a beam-synchronous stream [4]. Beam synchronous sources are connected to a realtime timing system that allocates an unique pulse-id to each shot passing through the beamline as well as readout triggers. The trigger initiates the data readout and the immediate attachment of the respective pulse-id. The sources then send out an atomic message containing the readout data along with the pulse-id. In this manner, the data of an electron bunch gathered across multiple BPM channels are sure to belong to the same shot.

2.2 The PCA Application

The aim of this semester project was to develop an compact application that allows for the acquisition of current beam operation data and the subsequent analysis of the gathered data set. Apart from basic orbit analysis such as rms orbit jitters and frequency analysis at each BPM, the main focus was put on the identification of collective jitter sources using PCA. The resulting python script is structured in three phases as can be seen in Figure 3.

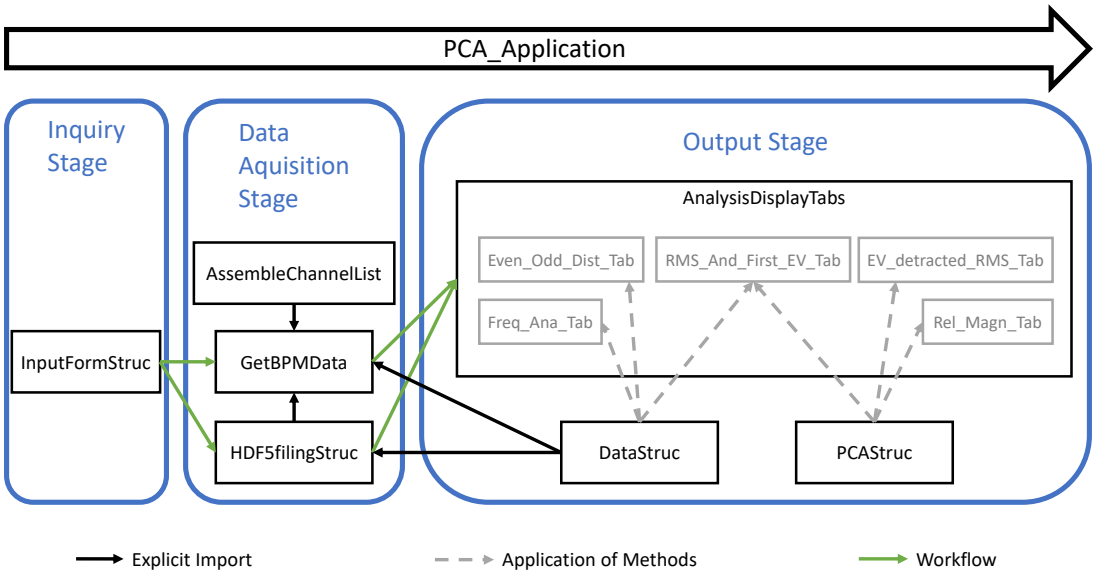

Figure 3: A schematic representation of the PCA application. The main file is *PCA_Application* and the top arrow represents the workflow within the script. All other files indicated by squared black boxes can be found in the *src* directory.

An input form inquires the type of input data as well as the desired data output. The GUI was programmed through the *tkinter* package, a GUI framework that is built into the Python standard library with the advantage that it is cross-platform. Out of the three possible layout managers in *tkinter* (*pack*, *grid* and *place*), the input form is structured through a single column grid with three rows as can be gathered from Figure 4. Each of the cell is then in turn structured by a grid. The first cell concerns the input data with the options to either generate a new data set or use an existing one. The sample size (or the amount of recorded shots) and the path to the

save directory can be customised with the defaults set to 5000 shots and the *Data* directory of the application. In the second cell, the user can tick the desired options for the analysis output with two options being customisable. Just as for the first cell, the default options are chosen if nothing is entered in the entry bars. The same principle is applied, if the Aramis or Athos channels input in the entry bars cannot be found in the channel list. The last cell contains the *Submit* -button, which prompts the input data to be collected and the *tkinter*-frame to be closed. The input form is implemented as a class with the initialisation invoking the input form frame.

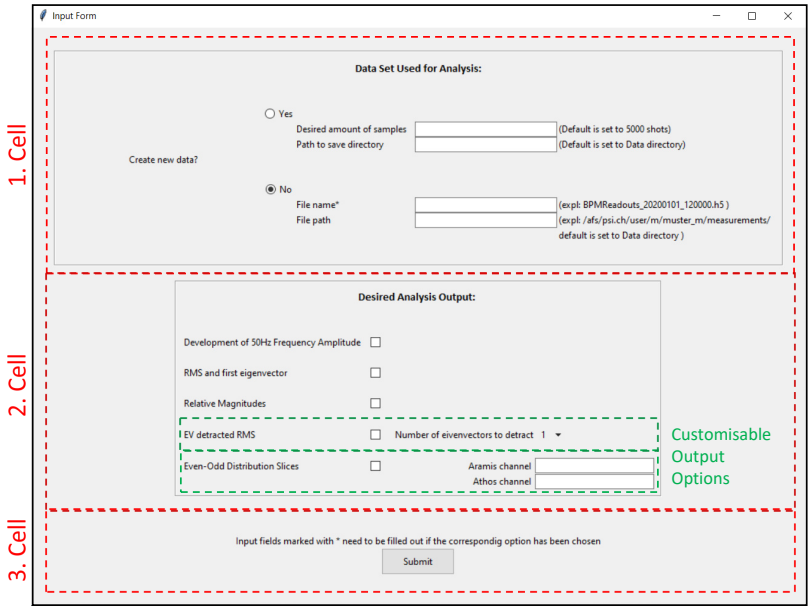

Figure 4: The input form displaying the user inquiry. The red dashed cells indicate the internal structure of the *tkinter*-frame using a grid as layout manager. The first cell concerns the type of input data for the analysis (newly generated or already existing data set). The second cell allows the user to tick the desired analysis output options. Lastly, the third cell contains the button to collect the user input and collapse the input form window. The green dashed boxes show the customisable analysis options.

The *InputForm* object is then passed to a switch-like structure implemented through a tree of conditionals. If new data is required in the second stage of the program, the script calls the *generate_data* function in the *GetBPMData* file. It first gathers a positionally sorted list of currently available BPM channels through the *AssembleList* function in the *AssembleChannelList* file. Since SwissFEL operates with a two-bunch system, channels belonging to the Aramis line, driven by the first bunch, are designated by a *X1* and *Y1* ending to the BPM channel names for the x- and y-axis accordingly. In the same manner, the *X2* and *Y2* endings denote the second bunch belonging to the Athos line. All machine-related devices including the BPMs are designated through 15 character long strings, exemplified by one of the Aramis undulator channels "SARUN08-DBPM070". The list of channels is then passed to the stream via *bsread*. The *bsread* module is a python package developed in-house at PSI to handle beam-synchronous data [5]. After looping through single-shot readouts in a *while*-loop until the desired sample size is reached, the data is saved to an HDF5 file. The function then returns an *HDF5file* object. This class is used to save objects of the class *BPMData* to HDF5 files or generate such an object

from an HDF5 file. A graphical representation of the HDF5 file architecture produced in that manner can be seen in Figure 5. In turn, the *BPMData* class is the data format containing all the necessary information about a BPM data set. Its main variables are *xmat* and *ymat*, which are two-dimensional *numpy* matrices. The first dimension represents the pulse-ID of one shot among the data set, while the second dimension orders the available BPMs according to their z position. A referral such as e.g. [3,6] points to the 4th recorded shot of the 7th BPM. Additional variables such as the channel name list or the z position list serve to characterise the data set and are mostly used to generate graphs.

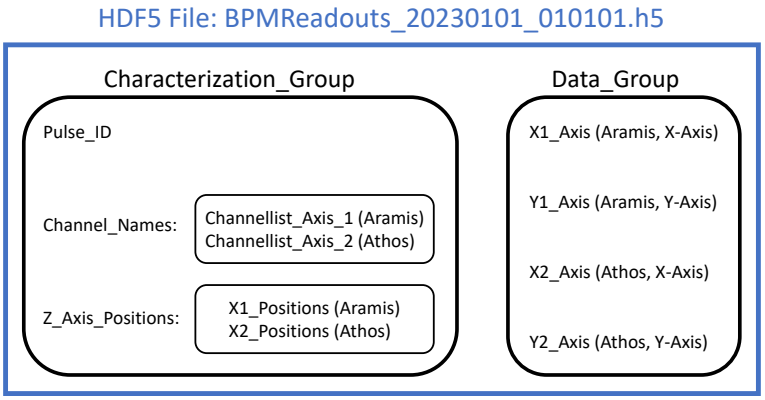

Figure 5: The data architecture of a HDF5 file output by the class *HDF5file*. Each of the black boxes represent a group or subgroup. The name of the example file follows the naming convention defined in the *GetBPMData* file and is generally used for this semester project. The *Data_Group* contains one *xmat* and *ymat* matrix for the each of the beamlines.

In the third stage of the program, the *HDF5file* object generated either by the *generate_data* function or through initialisation with the file name of an already existing data set is used to produce one *BPMData* object each for the Aramis and Athos line. A *tkinter* notebook is set up and for each type of analysis a notebook tab is initiated. The tabs themselves are subclasses to the *tkinter.Frame* class and mostly contain a 2x2 graphs collection along with a toolbar and a *Quit*-button. The methods for the PCA related tabs are contained in the separate *PCA* class. One feature that characterises this class is the *centred_data* variable, a matrix containing the data points of the x- as well as y-axis reduced by the data mean at each channel. Since each BPM channel can have an arbitrary offset and the PCA is only applied to centred data sets to avoid numerical artefacts, the mean at each BPM channel is taken as the point of origin. Other key variables in this class are *Vh* and *sigma*, which are explained in the corresponding subsection below. Each of the tab subclasses make use of class methods of *BPMData* and *PCA* to analyse the data set and display the result. The user can then comfortably switch in between tabs to have a look at the findings and customise as well as save the graphs via the toolbar. In order to safely exit the program, the *Quit*-button should be pressed.

The program can be run by plugging in the *PCA_Application* file along with the *src* and *Data* directories onto a computer within the SwissFEL network and running the *PCA_Application* file. Unless specified otherwise, the locally saved HDF5 file can be found in the *Data* directory. Since the bsread module needs to access the SwissFEL network, running the program without this access will result in an error. However, by slightly altering the *PCA_Application* script and disabling the option for the collection of new data (as well as the *GetBPMData* import

command), the application was also successfully run on an unconnected, Windows-based laptop. Depending on the desired sample size, the collection of new data may take some time. The default sample size of 5000 shots would take at best 50 s to gather when the machine runs at its maximum repetition rate of 100 Hz. There is an overhead for establishing the connection for the beam-synchronous readout. Most of the analysis modes in the output stage can be executed fairly fast. However, the singular value decomposition needed for the PCA requires a bit of time, because the data sets are usually fairly large. A previous study in PCA application on BPM data indicated, that the SVD execution time scales roughly with the square of the sample size for data sets above 1000 shots [6]. This is due to the fact that the shape of the data matrix becomes highly asymmetric with larger sample sizes. For example, the default sample size during standard operations of SwissFEL (in April and May 2023) produced an SVD input matrix of dimensions 5000×236, as is elaborated in Section 3. For symmetric input matrices, the SVD execution time is not expected to scale with the squared sample size. Furthermore, the same study also investigated the appropriate sample size through the convergence of the first two eigenvectors with growing sample set size. Beyond 4000 samples the change in the first eigenvectors does not amount to more than 0.1% in length. With the default sample size designated for this semester project at 5000 shot, the execution of the SVD could take up to 10 s. This is the reason why the switch tree discerns between tabs relying on the *PCA* class and the ones which do not. If the user does not want any of the PCA containing tabs displayed, the notebook can be output much faster in this way. Furthermore, especially the *HDF5file*, *BPMData* and *PCA* classes are structured in a modular way, allowing for an individual employment outside of the PCA application. The graphs and analytical results in the following section have all been produced using locally stored data along with class functions from the three classes.

3 Results

This section discusses the data set and the derived output using the python programs described above on an exemplary measurement. The data was taken during the morning on April 28th 2023, shortly after SwissFEL was started up after the scheduled shutdown period. A total of 5000 shots were recorded across all the active BPMs of the Aramis (118 BPMs) as well as the Athos line (121 BPMs). The the results presented here only focus on the Aramis line to avoid a lengthy discussion, but the data produced at the Athos line can be found in appendix B.

3.1 Basic Orbit Analysis

After accounting for the arbitrary offset by detracting the channel mean from the corresponding data points, the variation in transversal beam position is reasonably small. The largest absolute deviation of about 290 μm from the data mean can be found in the beam dump section. There, the deviation arises almost exclusively in the vertical plane. A considerably smaller absolute deviation of about 106 μm that mostly occurs in the x-axis can be found in the energy colimator section (SARCL02-DBPM260). As can be gathered from Figure 6, this pattern can also be observed in the rms.

3.1.1 Root Mean Square (RMS)

The root mean square in the case of discreet data sets such as this one departs from the standard deviation (std) only in the degrees of freedom that it needs to account for. However, since the data set used in this analysis sampled 5000 shots, there is virtually no difference between rms

and std. This is also the reason why the *numpy.std* method was used to compute the rms for this analysis.

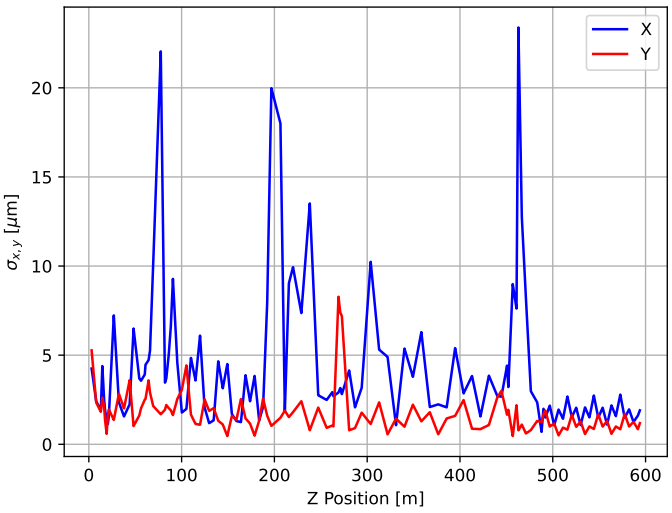

Figure 6: The root mean square (rms) across the Aramis line. The two BPMs installed at the beam dump have been removed from the graph, since the spike in the y-axis at this section distorted the graph too much. The full plot can be found in appendix A.

Just as with the absolute deviations from the mean, the rms is reasonably small across the beamline. The biggest variations can be found again in the beam dump (SARBD02-DBPM040) with an rms around 79 μm on the y-axis and the dipole colimator (SARCL02-DBPM260) showing an rms of 23 μm on the x-axis. It needs to be mentioned however, that the rms in the beam dump is more than 3.5 times as big as the rms in the rest of the beamline. As can be seen in Figure 6, three distinctive spikes can be made out on the x-axis. The first one belongs to the first bunch compressor (SINBC02-DPBM320), the second one to the second bunch compressor (S10BC02-DPBM140) and the third one to the energy colimator (SARCL02-DBPM260). Apart from the beam dump, the variation on the y-axis is on average smaller. Though there is a peculiar spike at around the bunch kicker (S20SY02-DBPM080). This might be because a CBPM38 model is installed at this point, which uses a bigger aperture (38mm) and thus has a lower resolution.

To get a tangible view of the data spread, shot distribution slices of two BPM channels have been provided in Figure 7. The data points have been sorted into bins with every other shot sorted into either the even or odd bin. The first shot has arbitrarily been assigned to the even bin, while the second one was then sorted into the odd bin. As can be seen in both subfigures, there is a distinct departure between the two data clouds. This occurs due to the 50 Hz main power supply to SwissFEL. Electron bunches are generated at a 100 Hz rate. Ideally, the electron bunch production would thus take place at each zero point of the sinusoidal wavefunction. However, smaller deviations induce a phase delay, effecting a slight shift to either a rising or descending slope. The main driving components are magnets and RF installations causing the grouping of the orbits into even and odd shots. This in turn produces this distinct pattern in the distribution. Though as can also be gathered from the rms development, this group difference does not worsen across the beamline.

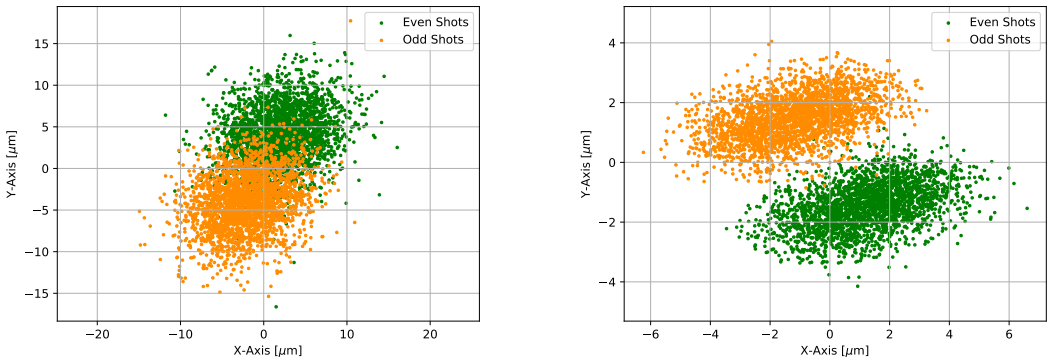

(a) Even-odd distribution for the channel SINEG01-DBPM340 in the Aramis line. It is the very first BPM installed in the injector section, where the installations are operated for both lines.

(b) Even-odd distribution for the channel SARMA02-DBPM020 in the Aramis line. This BPM is located in the single bunch section right before the bunches enter the undulators.

Figure 7: Distribution slices of shot positions measured by two BPMs in different sections of the beamline. The shots have been grouped in two bins, with every other shot belonging to one group. The group designation of even and odd was chosen arbitrarily.

3.1.2 Frequency Spectrum Analysis with FFT

Since the distribution slices in the previous subsection implied systematic deviations characterised by the 50 Hz frequency, a general investigation into frequency contributions to data variation might be of interest. Fast Fourier transformations (FFT) provide a useful tool for a discreet spectral components analysis on data samples. Because the discrete Fourier transformations on real input produces frequency terms that are Hermitian-symmetric, the negative frequency amplitudes correspond to the complex conjugates of the positive frequency amplitudes. The frequency amplitudes of the negative frequency spectrum is therefore determined by the results of the positive frequencies and vice versa. The *numpy* package provides useful and efficient methods for FFTs. For that reason *numpy.fft.rfft* has been used to apply an FFT on the x- as well as the y-axis data set. It outputs only the amplitudes of the positive frequency spectrum and for a data set containing k data points it outputs $\frac{k}{2} + 1$ for an even k and $\frac{k+1}{2}$ frequency amplitudes for an odd k. The highest frequency that can be resolved is dictated by the Nyquist theorem, whereby the sampling rate to reproduce a pure sine wave measurement must be at least twice its frequency. Since the electron bunches are produced at a 100 Hz rate, the largest possible frequency output by the FFT is 50 Hz. In connection with the amount limitation on frequency amplitudes, the frequency resolution of the FFT is then given by the duration of the measurements. For 5000 shots at 100 Hz this corresponds to about 0.02 Hz.

An example of a spectral component analysis can be found in Figure 8. The graph displays the frequency amplitudes for a BPM channel in the undulator section of the Aramis line. Most striking are the singular spikes at the 16.7 and 50 Hz frequencies for the x- and the y-axis alike. The spectral composition of the data distribution differs from channel to channel, but clearly distinguishable and major peaks in those two frequencies can be found in almost all of them. The spike in the 16.7 Hz frequency can be traced back to the Swiss Federal Railways (SBB). The electric supply networks for the trains is operated at 16.7 Hz, so nearby SBB facilities exert an influence on SwissFEL. This noise is particularly present in the morning and in the evening

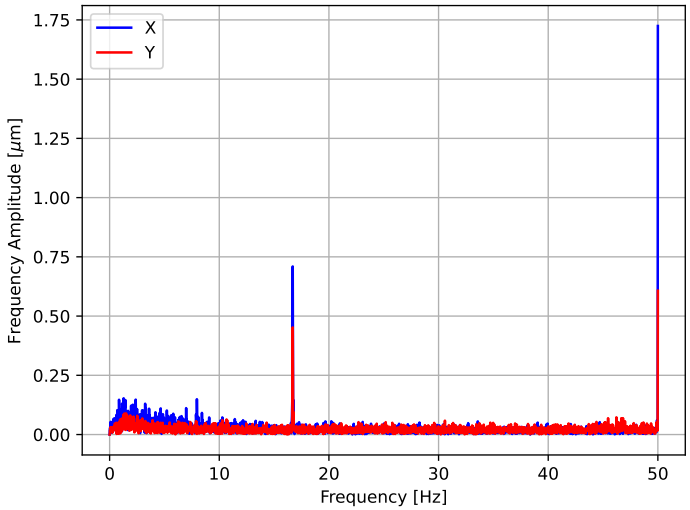

Figure 8: Frequency spectrum of a BPM channel in the undulator section (SARUN09-DBPM070) of the Aramis line. The 0 Hz frequency is set to zero since the amplitudes are regarded in the center of mass system.

during work week rush hours. The cause of the other dominant peak at 50 Hz is due to the bunch production rate of 100 Hz. As was shown in Figure 7, the shot distributions indicate a symmetric data spread around the coordinate origin in the centre of mass system. Assuming the shots to be produced at a local extremum of a sine with 10 ms passing in between them, the total period of this sinusoidal wave is $T = 20\,\text{ms}$ in total.

Since the 50 Hz frequency plays a dominant role in explaining data variation, the development of the 50 Hz frequency amplitude is of particular interest. A good measure of its importance is the relative magnitude in comparison to the total amplitude A_{tot}. If a_j is the frequency amplitude for one particular frequency j, the oscillation in the x-axis at one BPM for example is given by $x(t) = \sum_j a_j sin(\omega_0 jt)$. The term ω_0 describes the minimum non-zero frequency. For the data set analysed here, this corresponds to $\omega_0 = 0.02\,\text{Hz}$ as derived above. The rms jitter is thus given by $\sigma_x = \sqrt{\int_T dt \cdot x(t)x^*(t)}$, which is the $||L||_2$ norm. The term $x^*(t)$ follows the convention to denote the complex conjugate with an asterisk. Because the rms considers the data points only with respect to the data mean, the system is regarded in the centre of mass system. Consequently, the amplitude of the 0 Hz frequency is neglected, since for the data mean $< x(t) >= \int_T dt' \cdot x(t') = 0$ needs to hold in the centre of mass system. The total amplitude can then in reference to the rms be characterised in the following way:

$$A_{tot} = \sqrt{\sum_{j,k=1} \int_T dt \cdot a_j a_k^* \sin(\omega_0 jt) \sin(\omega_0 kt)} = \sqrt{\sum_{j=1} \frac{1}{2} \cdot |a_j|^2}$$

It needs to be mentioned, that since *numpy.fft.rfft* outputs only half of the spectrum and the frequency amplitudes are input as absolute values, the factor $\frac{1}{2}$ was neglected for the computation of the sum over all frequencies. One of the tabs that can be generated by the PCA application shows the relative amplitude of the 50 Hz frequency for both axis on both lines. There, the

50 Hz amplitudes resulting from the FFT applied on every BPM across the beamline is displayed normalised by the total amplitude. Figure 9 shows the graphs resulting from this analysis on the Aramis line.

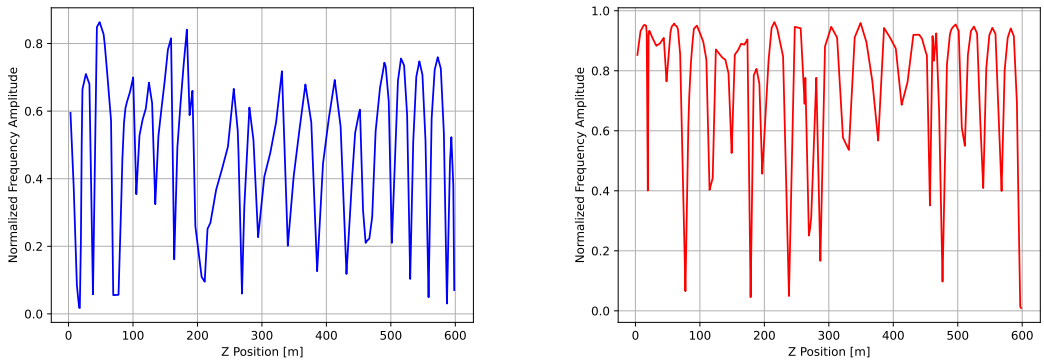

(a) Frequency development on the x-axis.

(b) Frequency development on the y-axis.

Figure 9: Development of the relative share of the 50 Hz frequency amplitude on the Aramis line. The data points have been obtained through performing an FFT on each BPM channel.

In the graphs, the share of the 50 Hz jitter component rises and decreases with a certain periodicity across the beamline. Similar beam behaviours can be found along a betatron or other particle accelerators when the orbit is exited by an initial offset or angle. The betatron oscillation describes a movement transversal to the beam propagation direction, whereby particles oscillate around the reference orbit [7]. This behaviour can be described by a cosine-like function with the amplitude $\sqrt{\beta(z)}$ being dependent on the longitudinal z position along the accelerator beamline. Observing the multitude of electron bunches passing across the beamline, they depict a very distinct pattern of repeated focusing towards the reference orbit and their divergence from it. This is due to the discreet placement of beam focus elements such as quadrupoles. It is highly impractical to apply a continuous focusing. Instead, focusing is exerted on the beam discretely at specific intervals. Those circumstances are mirrored in the beam orbit, as the electrons get accelerated towards the reference orbit and then overcompensate in the opposite direction after the focusing element in a periodic manner. If the 50 Hz jitter is generated at a specific location, the beam jitter variation follows closely the beam orbit with observable maxima and minima. At a local minimum, the jitter is focused onto the reference orbit and thus "hidden" in the orbit divergence (dx or dy), which is why it cannot be picked up by the individual BPMs. Seeing as the peaks of relative share of the 50 Hz amplitude are often around 75 to 95%, the displacement due to betatron oscillation accounts to the biggest share in the variance between shots. However, slight deviations from the periodic patter such as the wider gap and slanting increase of the amplitude share at around 230 m in Figure 9(a) might indicate, that the jitter source has other contributions beside the systematic 50 Hz jitter. The next subsection therefore looks at the results from the PCA and what possible jitter sources could be identified through it.

3.2 Principal Component Analysis (PCA)

Principle component analysis is normally used in machine learning to reduce the dimensionalities (or features) of a given data set [8]. If a data set is approximately aligned with a manifold of

lower dimensionality, the excess information can be significantly reduced by projecting the data set onto the manifold. As was discussed above for the the data set analysed in this report, the deviations from the reference orbit are of the order of micrometers. The small scale of the orbit jitter allows that the transport of the electron beam, insofar as it deviates from the ideal orbit, can be described by linear algebra. Higher order effects, e.g. the impact of sextupole magnets are considered to be negligible for this study. In this case, the manifolds characterising the linear jitters are expected to be hyperplanes.

The positional variations in the beam orbits are typically correlated among each other [6]. Regarding the variations for each BPM individually would therefore neglect collective movements across the beamlines. This also implies, that the amount of independent variation sources is significantly smaller. The goal of a cumulative analysis (of all BPM data) is therefore to identify vectors characterising the hyperplane which describes most of the variation in the positional data. PCA preserves variance by extracting projections that conserve the maximum amount of variance [8]. The principal components are iteratively determined by minimising the mean squared distance between the axis and data points. Subsequent vectors are orthogonal and account again for the largest amount of remaining variance. PCA thus outputs the principal components as zero-centered unit vectors in order of their explanatory power for the data variance. Note that the origin of coordinate in PCA is set at the centre of mass (data mean). This is because data variation is regarded in reference to the data mean and not the arbitrary point of origin given by the BPM readouts. If the PCA is to output the vectors pointing in the directions of the largest variance, systematic errors need to be dealt with first by subtracting the the data mean offset from the data.

The principal components of a linear system can be found through singular value decomposition (SVD). The SVD decomposes a matrix A of dimensions $M \times N$ into a unitary matrix $U \in Mat_{\mathrm{M\times M}}$, a diagonal matrix $\Sigma \in Mat_{\mathrm{M\times N}}$ with non-negative numbers on the diagonal and an unitary matrix $V^H \in Mat_{\mathrm{N\times N}}$ [9]. The decomposition is therefore of the form:

$$A = U\Sigma V^H$$

The eigenvalues contained in Σ are ranked in descending order of their magnitude. The V matrix on the other hand arranges the eigenvectors representing the principal components in columns. In the context of this orbit jitter decomposition, each eigenvector corresponds to a single mode of machine jitter, constituting a linear slope in the N-dimensional vector space.

The script oft the PCA application implements the SVD through the *numpy* package. Contained in *numpy.linalg* is a dedicated method for SVD that outputs all three factorisation matrices. The SVD is based on the *xmat* and *ymat* data matrices of the *BPMData* class. However, the correlation analysis is performed simultaneously on the x- and y-axis of all the BPM channels. In the first place, the two axis have been treated separately thus far only for the sake of readability. A single jitter source can affect the orbit in the x and y direction simultaneously. The input matrix A for the SVD is therefore put together from *xmat* and *ymat* and of dimension M = [amount of recorded shots] and N = 2×[number of BPM channels]. The complexity for computing the SVD for such a matrix A is $\mathcal{O}(\min\{M^2N, MN^2\})$. Additionally, the eigenvalue decomposition is proportional to N^3, resulting in an overall complexity of $\mathcal{O}(MN^2 + N^3)$ for the PCA execution on data sets with large amounts of recorded shots [10].

Furthermore, the data set needs to be centred. The BPM data contains the absolute orbit position, while the PCA is realised in the centre of mass system (or the relative orbit position). Therefore, the mean value of each BPM channel is subtracted from the respective data points. In the PCA application, the *PCA* class is initialised from a *BPMData* object by first creating the *centred_data* matrix and then performing the SVD on this variable to set the Σ and *Vh* variables. The number of eigenvectors is limited by N, the double of the amount of BPM channels used to

generate the data set.

3.2.1 Relative Magnitudes

Among others, the SVD produces the diagonal matrix Σ containing the eigenvalues λ_i. In the context of orbit jitter, they can be used to estimate the impact of the different jitter sources. In order to put the eigenvalues in relation with each other, they can be compared to each other using the $||L||_2$ norm. This is because eigenvectors are orthonormal in the sense of the Euclidean space of the data set.

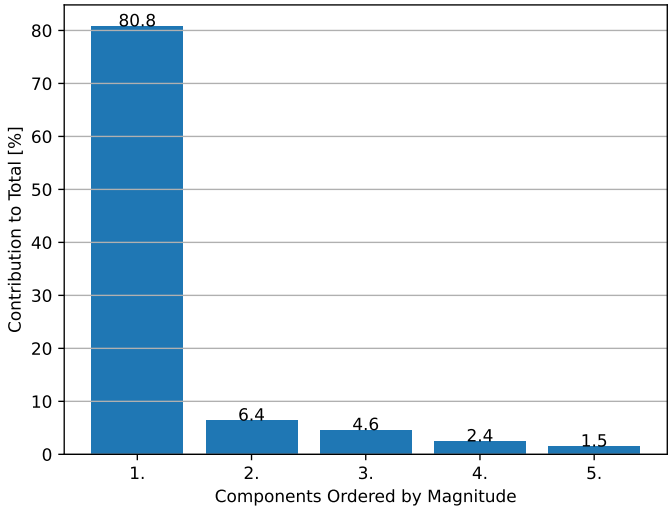

Figure 10: Proportional display of the magnitudes of the eigenvalues belonging to the principal components. The share of the eigenvalues has been computed using the L^2-norm squared. Only the first 5 pricipal components have been listed, since the rest amounted each to less than 1%.

The display of the relative magnitudes are part of the PCA application as well. The relative magnitudes of the different eigenvalues have been computed in the following way:

$$\Delta_{\text{rel}}\lambda_i^2 = \frac{\lambda_i^2}{\sum_{k=1}^{N} \lambda_k^2}$$

The application automatically selects the eigenvalues amounting to more than 1% and displays them in a bar chart. The output for the Aramis data set discussed in this report can be found in Figure 10. The first eigenvector contributes by far the most to the variation of the data, amounting to 80.8%. From the sixth mode onwards, the eigenvectors already contribute less than 1%. The fist five eigenvectors contribute 95.6% of to all of the jitter modes. The variation in the electron orbit is thus dominated by only 5 modes, which in turn are mostly represented by the first mode. The following sections will therefore only regard the first 5 eigenvectors for further analysis.

3.2.2 Evaluation of Jitter Modes

The collection of eigenvectors output by the PCA encode the propagation of perturbations. Especially the first eigenmode is of interest as it accounts for the most variation in the bunch orbit. Figure 11 gives a graphical representation of the first eigenvector in the centre of mass system. The beam dump section has been excluded from this figure for a facilitated comprehension of the plot. However, the complete eigenvector is shown in the appendix in Figure 15. The most striking observation is that the first eigenvector almost exclusively accounts for the jitter in the dump dipole with little activity in any other section in the vertical plane (y-axis). Though that is in agreement with the observation, that the jitter defining the readings at the dump BPMs also strongly dominates the rest of the rms behaviour in the beamline.

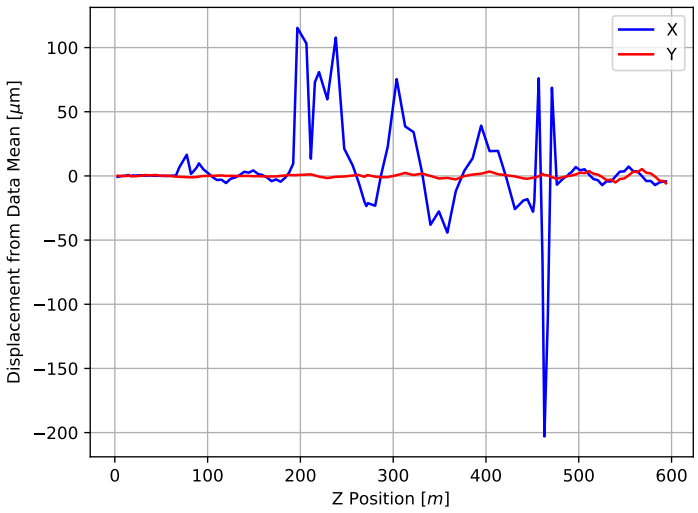

Figure 11: Graphical representation of the first principal component of the Aramis line. The BPMs in the beam dump section have been removed, since the spike in this area distorted the graph. The full eigenvector can be found in appendix A.

On the x-axis on the other hand, the eigenvector is only initially inactive up until the first bunch compressor. Small displacements can be seen at this point and the eigenvector oscillates with a minor amplitude through the first linac afterwards. A first considerable activity can be made out at the second bunch compressor, followed with an oscillatory movement through the second and third linac. Finally, a distinct spike and strong fluctuations can be observed in the energy colimator section. Especially in the area of the second bunch compressor and the energy colimator, the first eigenvector overlaps with the locations of increased rms. However, it shows little displacement at the first bunch compressor, the area identified with the first spike in the x-axis rms. In general, the first eigenvector shows much more varied behaviour in the x-axis than the y-axis, but is commonly active in sections associated with rms spikes.

Since the eigenmodes are orthonormal, they constitute a basis of the $\mathbb{R}^N$ vector space. The share each of them take in the constitution of a given data vector can be calculated by projecting the data vector onto the eigenvectors. If $\vec{r} \in \mathbb{R}^N$ designates a data vector generated by one shot and $\vec{p}_i \in \mathbb{R}^N$ the ith eigenvector, the contribution of the ith eigenvector can be subtracted from

the entire data set through the following equation:

$$\vec{r}_{red,i} = \vec{r} - (\vec{r} \cdot \vec{p}_i)\vec{p}_i$$

This procedure can be extended to all of the data vectors of a data set. The difference between the original rms and the rms of the reduced data then constitutes the aggregated contribution of the specific eigenvector.

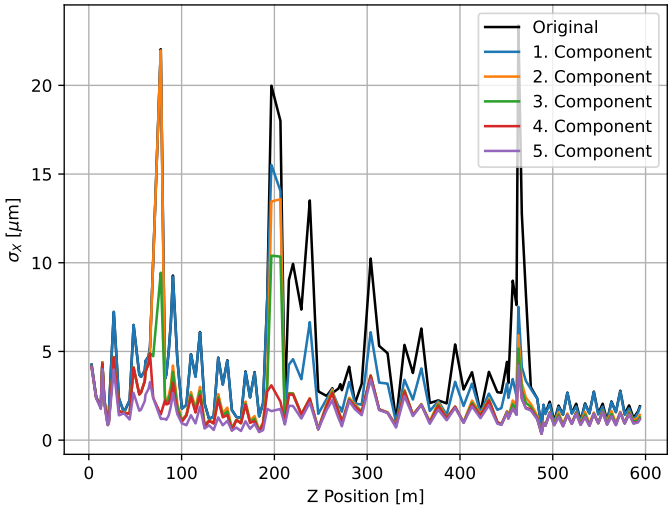

Figure 12: Eigenvector detracted rms specifically on the x-axis of the Aramis line. The reduction of rms by subtracting the contribution of the first five jitter modes from the data is displayed for the whole length of the beamline.

The analysis option "EV detracted RMS" outputs a sequential detraction of eigenvector contributions. Figures 12 and 13 show the results specifically for the Aramis line. In most of the beamline, the rms gets reduced to bellow 4.2 μm by just detracting the influence of five jitter modes. Interestingly, it stays consistently at around 8 μm on the y-axis at the bunch kicker. In the rest of the beamline, the rms is already below the maximum position noise level for the CBPM38 and CBPM16 models. For small residual values the signal is dominated by the processing noise of the BPMs and variations in the positional data can no longer be associated with collective jitter sources.

As can be seen in Figure 16, the first eigenmode is responsible for almost entirely rectifying the spike in the beam dump, but has little influence elsewhere on the y-axis. Other jitter components contribute weakly to y-axis variations across the whole beam line. A more complex picture can be derived from the x-axis in Figure 12 however. As was discussed above, the contribution of the first jitter mode only really starts at the second beam compressor with the largest influence being exerted at the energy colimator. The second jitter mode is present over the whole beamline, but nowhere in a dominating way. Most interestingly, the influence of the third component can be identified in exactly two spots: the first and the second bunch compressors. Which is same behaviour indicated by the fourth eigenvector. The fifth component, much like the second one, exhibits minor, but consistent contributions across the beamline. The next section thus discusses,

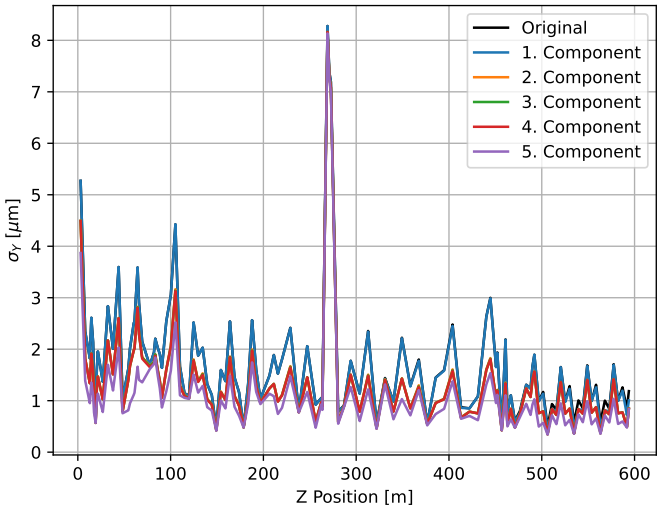

Figure 13: Eigenvector detracted rms specifically on the y-axis of the Aramis line. Since the beam dump section showed a strong peak in the original rms, the beam dump BPMs have been removed from the z position axis.

in what way the observations about the jitter mode behaviours are to be interpreted and what conclusions can be drawn in regards to the jitters sources.

4 Discussion

The rms as well as the first eigenvector indicated a large spike in the beam dump section. Since this disproportional magnitude of variation occurs after the intended use of the electron bunches, the question arises how it needs to be regarded for the interpretation of jitter sources. The behaviour of electrons in the beam dump section is heavily correlated with variations in the energy, because a large dipole magnet deflects the spent electron beam downwards into the dump. A change in electron energy alters the deflection angle and becomes visible as an orbit deviation after some distance. The first eigenvector largely deals with the data variation in the beam dump section, what hints to a strong association with energy jitter. This does not mean that the first jitter mode solely relies on differences in the energy and other sources of influence might still play a role. But seeing as the rms spike is mostly diminished by the first eigenvector, the main jitter mode is certainly determined by energy variations to a large extend. Furthermore, since the relative magnitude of the first eigenmode suggests a contribution of around 80% to the system, the dominating effect in the whole of the beamline can be expected to be energy jitter. This argument is also supported by the fact that the other dominant parts of the first eigenvector are localised in dispersive regions of the horizontal plane, where also an energy dependent variation in the orbit by an energy jitter is expected: namely the two bunch compressors and the energy colimator. In that sense, the peak in the beam dump section is not required for the localisation of jitter sources, but for the determination of this specific , energy driven jitter type. However, it still needs to be mentioned, that an overwhelming share in regards to the relative magnitude of the first eigenvector is also due to the large spike in the beam dump and as such, the PCA is

biased towards the largest jitter source. This is reasonable, since we are looking for the sources of the most significant orbit jitters. On the other hand, a different strategy would be to first normalise all BPM data by the corresponding rms amplitude in order to avoid bias towards a few large observed jitter locations. Though, in this case the interpretation gets much more difficult.

Energy jitters are not necessarily active from the very beginning of the beamline, unlike positional variances. They can exert only weak or no influence at all on the electron orbit up until sections, in which the bunch energy assumes a major role in the determination of the trajectory leading to orbit jitters due to the energy. This would apply to beamline sections like the bunch compressors, the energy colimator and as mentioned above, the beam dump. This distinct behaviour can also be recognised in Figure 11. The first eigenvector is not active at all until the first bunch compressor and starts to indicate major displacements at the second bunch compressor. Comparing this insight to the rms in Figure 6 provokes the question, why the first jitter does not contribute more to the variation in the first bunch compressor, despite the large spike in rms in that region. For one, the linacs might be responsible for producing energy jitters. The first bunch compressor succeeds the injector area and is followed by the first linac. It can therefore be possible that the acceleration in the first or subsequent linacs may produce energy jitters by way of inhomogeneous acceleration of electron bunches. Another possible reason why the energy jitter is only clearly visible from the second bunch compressor onwards is that the energy dispersion is not closed in this section. Bunch compressors cause the electron bunch to become more compact by way of path length difference. Lower energy electrons like the ones leading in the bunch describe a longer bypass trajectory compared to the higher energetic ones located in rear. Optical elements in the bunch compressor like quadrupoles are used to correct for any spatial tilt. Thus it is a compromise between an aligned electron beam and induced orbit jitter due to leaked dispersion. A third explanation is the impact of coherent synchrotron radiation in the bunch compressor system. The bunch length is the shortest at the end of the magnetic chican and thus can emit coherently over the broadest wavelength spectrum of the synchrotron radiation. Thus it has its strongest energy loss there, while the dipoles are configured for unchanged beam energy. The mismatch between beam energy and design energy could cause some leaked dispersion similar to the quadrupoles for tilt correction. Note that the PCA is the first step to indicate the source of jitter. Dedicated studies should follow to discern between the possible origins of the jitter.

Interestingly enough, the prime jitter mode oscillates after the first considerable peak in the second bunch compressor, but the amplitude decreases continuously until the energy colimator. This might be caused by the acceleration in the subsequent linacs. During acceleration processes, the transversal momenta p_x and p_y are conserved, while the momentum along the beamline p_z is significantly increased. The trajectory slope $\frac{p_{x,y}}{p_z}$ thus decreases, a mechanism called adiabatic damping. It causes the oscillation around the reference orbit due to the energy jitter to gradually flatten out.

All of the observations thus far have been concerning the behaviour of the first jitter mode in the x-axis. Apart from the beam dump section, it shows very little activity on the y-axis. Though, the rms on the y-axis is generally small in the first place. The same extensive discussions could be held in regards to the second and third eigenmodes as well. As explained above, the first eigenvector points in the N-dimensional direction of the largest variation in the data set. Since all of the eigenvectors are orthogonal to each other, subsequent eigenvectors are set up in reference to the first one. They are thus not completely independent of the first mode, making it difficult to discuss them entirely on their own merits.

Taken together, absolute deviations and the rms across the beamline are generally small. A distinct delta peak at 50 Hz observed by the FFT across the beamline indicates, that much of the variance can be explained by the main power supply to SwissFEL and its influence on the

electron bunch production. The periodic in- and decrease in the share of the 50 Hz amplitude throughout the line can be attributed to betatron oscillation caused by the discreet placement of beam focus elements. In the PCA, the first jitter mode contributes by far the most to the positional variations in the data set. The spike of the eigenvector in the beam dump section of y-axis implies, that it can be characterised as an energy jitter. The peaks on the x-axis in the areas of the second bunch compressor and energy colimator suggest a dispersion leakage in those sections or the linacs as possible jitter sources.

Further investigations could entail a separate PCA specifically neglecting the beam dump area. This would also serve to estimate the importance of the first eigenmode if the considerable peak in this section is already accounted for. The influence of optical elements in the bunch compressors could be checked by switching off the quadrupoles in that part. Furthermore, some of the BPMs are equipped to measure the energy of the electron bunches. If the dependence of the orbit on the energy is measured across the beamline, a more detailed map of high energy dispersion areas could be gained. Lastly, the correlation analysis could be extended to include the Athos line as well. This way, the jitters arising from the shared infrastructure might be more easily identifiable. In any case, closing the energy dispersion could greatly reduce energy jitters and improve the SwissFEL performance.

In general, SwissFEL operation produces a wealth of data without infringing on the photon emission process. Applying isolated statistical observations of beam position measurements would neglect correlated fluctuations. Instead, PCA represents a highly intriguing approach by regarding the interdependencies of the vastly differing functional entities across the beamline. It allows for an extensive insight in the localisation and variation contribution of jitter sources. As a result, it deepens the understanding about the factors that are at play in the emergence of fluctuations. The achieved information from the PCA analysis will be the foundation to improve SwissFEL by localising jitter sources and spending a dedicated effort to minimise their impact. This insight cannot be achieved by analysing BPM data only individually. However, this semester project has not exhausted the applicabilities of PCA and more advanced implementations could certainly benefit the informative value of SwissFEL data.

Acknowledgements

I would like to give my cordial thanks to Dr. Andreas Adelmann and Dr. Sven Reiche for the opportunity of this exciting semester project and the most patient guidance. Without this support, this project would not have been completed. Gaining a fraction of the extensive knowledge required to make a large-scale research facility such as SwissFEL work was an interdisciplinary challenge. Without the generous help of multiple technicians and researchers at PSI, this semester project would certainly not have provided the learnings and the personal successes that it has.

References

[1] C. J. Milne, T. Schietinger, M. Aiba, *et al.*, "SwissFEL: The Swiss x-ray free electron laser," *Applied Sciences*, vol. 7, no. 7, pp. 720–, 2017.

[2] E. Prat, R. Abela, M. Aiba, *et al.*, "A compact and cost-effective hard x-ray free-electron laser driven by a high-brightness and low-energy electron beam," *Nature Photonics*, vol. 14, pp. 48–754, 2020.

[3] B. Keil, R. Baldinger, R. Ditter, *et al.*, "Status of the SwissFEL BPM system." `https://accelconf.web.cern.ch/ibic2015/papers/tupb065.pdf`, last access: 05.06.2023, 2016.

[4] H. Ebner, S. G.and Brands, Kalantari, *et al.*, "SwissFEL- beam synchronous data acquisition – the first year." `https://accelconf.web.cern.ch/icalepcs2017/papers/tucpa06.pdf`, last access: 05.06.2023, 2017.

[5] PSI, "Bsread python implementation." `https://github.com/paulscherrerinstitute/bsread_python`, last access: 05.06.2023, 2022.

[6] S. Reiche and E. Ferrari, "Orbit jitter analysis at SwissFEL." `https://indico.jacow.org/event/44/contributions/496/`, last access: 05.06.2023, 2021.

[7] K. Wille, *Physik der Teilchenbeschleuniger und Synchrotronstrahlungsquellen.* Stuttgart, Germany: Teubner Studienbücher, 1996. ISBN: 9783519130871.

[8] A. Géron, *Hands-on Machine Learning with Scikit-Learn, Keras and Tensor-Flow.* Sebastopol, California: O'Reilly Media, Inc., 2019. ISBN: 9781492032649.

[9] A. K. Cline and I. S. Dhillon, "Computation of the singular value decomposition," in *Handbook of Linear Algebra* (L. Hogben, ed.), pp. 45.1–45.13, New York, NY: Chapman and Hall/CRC, 2006. ISBN: 9783519130871.

[10] P. Viviani, M. Drocco, and M. Aldinucci, "Scaling dense linear algebra on multicore and beyond: A survey," in *Proc. of 26th Euromicro Intl. Conference on Parallel Distributed and network-based Processing (PDP)*, pp. 751 – 758, IEEE, 2018.

A Full Aramis Graphs

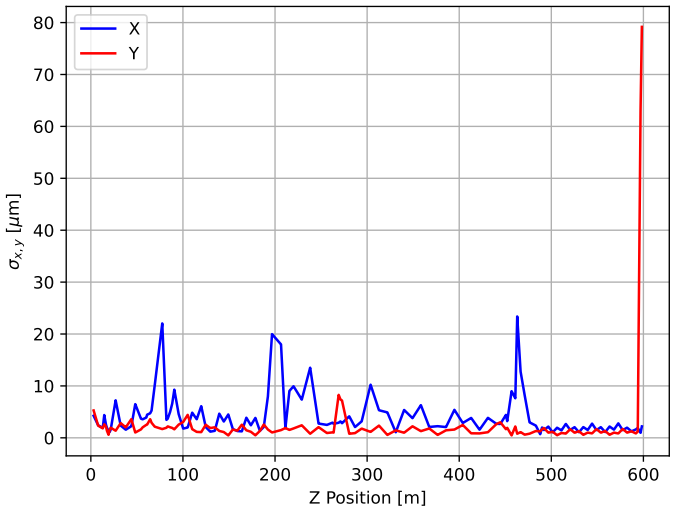

Figure 14: Root mean square at every BPM channel across the Aramis beamline including the beam dump

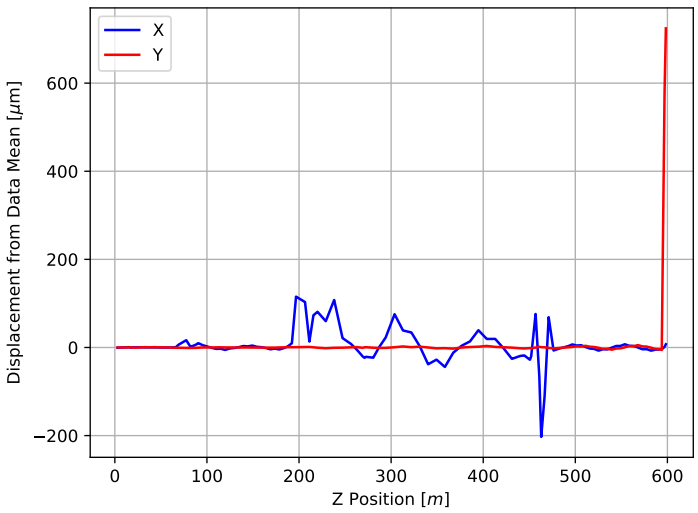

Figure 15: Graphical representation of the first principal component output by the PCA. Unlike Figure 11, this graphs also includes the beam dump section of the Aramis line.

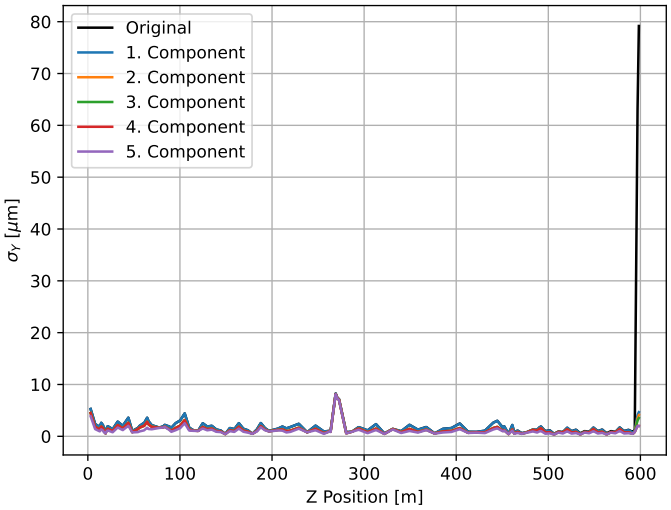

Figure 16: Eigenvector detracted rms on the y-axis of the Aramis line. This graphs includes the beam dump section as well. The first eigenmode largely accounts for the variation at the beam dump.

B Analytical Output for the Athos Line

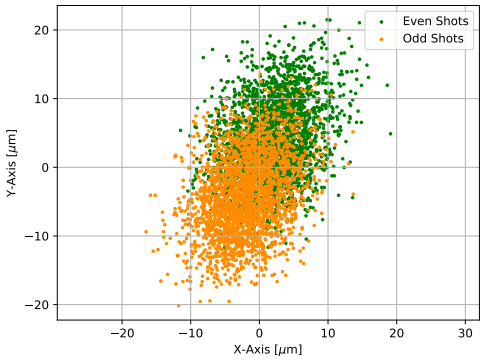

(a) Data point distribution for channel SINEG01-DBPM340. This is the very first BPM in the Athos line located in the injector, where the beamline is operated in the two-bunch mode. The origin of the coordinate system is set to the data mean.

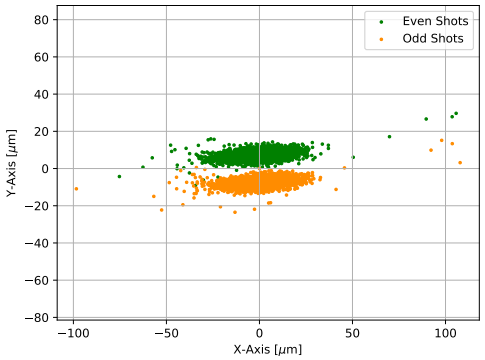

(b) Data point distribution for channel SATMA01-DBPM602. This is a BPM in the single bunch section right before the undulators. The distribution has a few outlier in the x-axis. This increased variance is also visible in the rms in Figure 18(a).

Figure 17: Even-odd distribution slice of the beam positions at two different BPMs of the Athos line. The even or odd designation is given to every other shot, but the assignment of the first shot was given on an arbitrary basis.

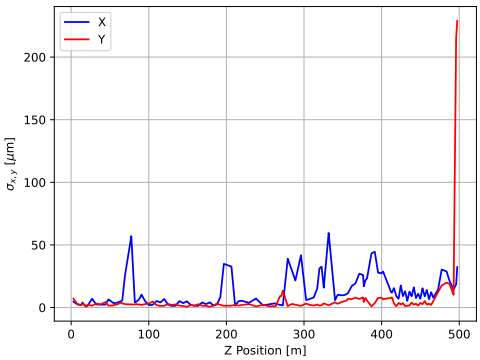

(a) The rms development across the whole of the Athos line. Much as in the Aramis line, there is a disproportionally large peak at the beam dump. However, there are subtle differences like the increased rms on the y-axis in the last parts of the beamline. The peaks in the x-axis at the bunch compressors are now much more isolated.

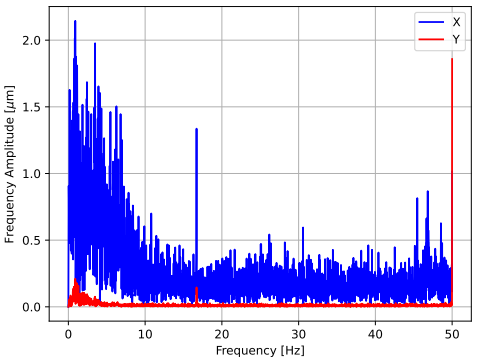

(b) The frequency spectrum of the Athos BPM corresponding to the one of the Aramis line in Figure 8 (SARUN09-DBPM070). The amplitude distribution is not as distinct as the one in the Aramis line. However, pronounced peaks at the 16.7 and 50 Hz frequencies are still visible in the x- as well as the y-axis, even if they contribute to a different degree.

Figure 18: The rms and the frequency analysis performed on the soft X-ray line Athos.

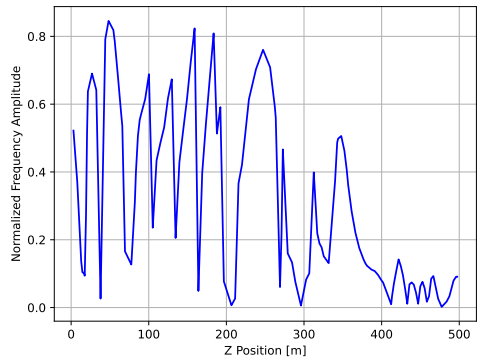

(a) Frequency development on the x-axis. The oscillatory pattern is preserved, but there is a clearly decreasing trend of the amplitude. This strongly suggest, that other jitter sources are more dominant in the latter beamline sections.

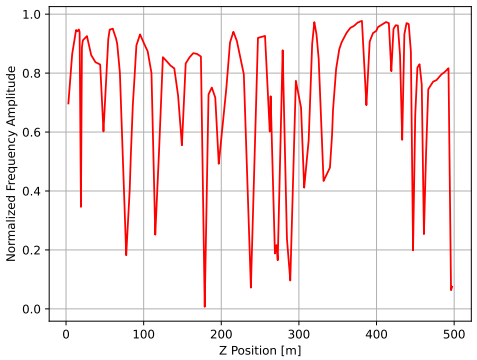

(b) Frequency development on the y-axis. Much as in the Aramis line, the amplitudes oscillates quite regularly in the y-axis. This indicates, that much of the variation can be explained by the bunch generation rate and the SwissFEL power supply

Figure 19: The development of the 50 Hz frequency amplitude across the Athos line.

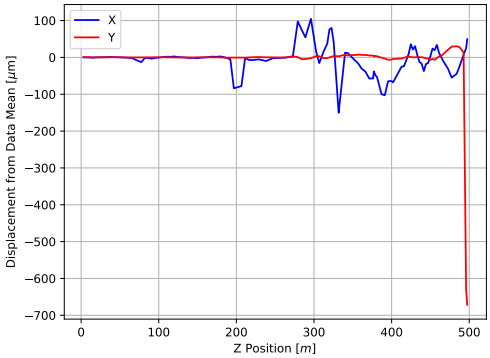

(a) Graphical representation of the first principal component on the Athos line. Just like in the Aramis line, it shows little activity on the x-axis at the first bunch compressor, unlike the second one and the energy colimator. There is also a disproportional delta peak at the beam dump, but in the negative direction.

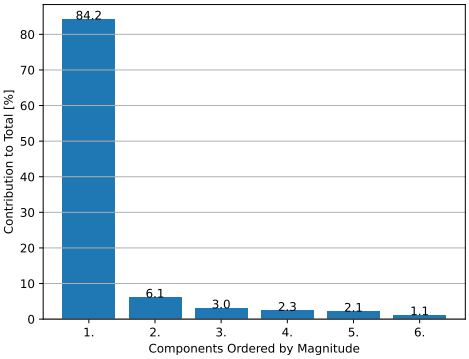

(b) Relative magnitudes of the first 5 components. The first eigenvector contributes even more to the data variation than for the Aramis line. However, there are six eigenvectors amounting to more than 1%. Though, the third until the sixth eigenvector account to approximately the same degree to the data variation.

Figure 20: First results of the principal component analysis performed on the Athos line.

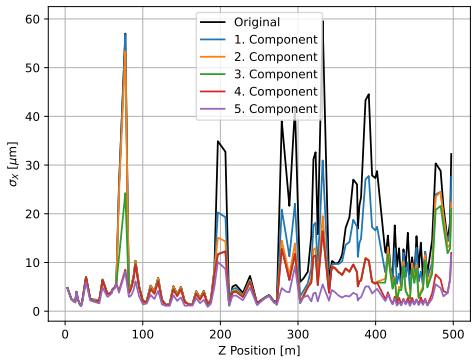

(a) Eigenvector detracted rms specifically on the x-axis. The behaviour is similar to the Aramis line. However, no oscillation takes place by the first eigenmode after the second beam dump, unlike after the peak at the energy colimator.

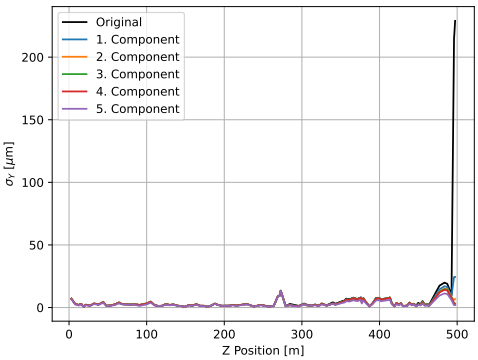

(b) Eigenvector detracted rms specifically on the y-axis. The first eigenvector mostly deals with the spike in the beam dump. Though unlike in the Aramis line, it is also active in the undulator section.

Figure 21: Display of the reduction of rms by subtracting the contributions of the first five jitter modes from the data of the Athos line.